AIP | Applied Physics Letters

Tunable thermoelectric transport in nanomeshes via elastic strain engineering

Brian Piccione and Daniel S. Gianola

Citation: Applied Physics Letters **106**, 113101 (2015); doi: 10.1063/1.4915270
View online: http://dx.doi.org/10.1063/1.4915270
View Table of Contents: http://scitation.aip.org/content/aip/journal/apl/106/11?ver=pdfcov
Published by the AIP Publishing

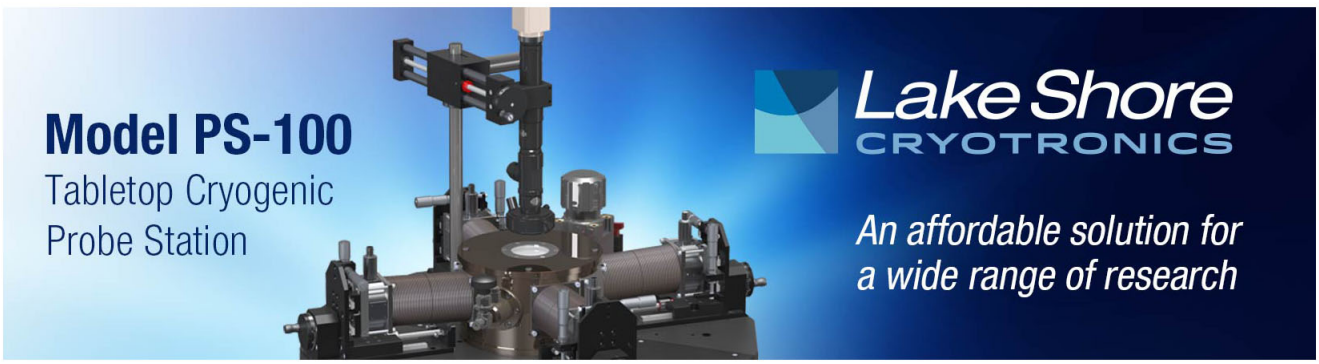

Tunable thermoelectric transport in nanomeshes via elastic strain engineering

Brian Piccione and Daniel S. Gianola[a)]
Department of Materials Science and Engineering, University of Pennsylvania, Philadelphia, Pennsylvania 19104, USA

(Received 8 December 2014; accepted 6 March 2015; published online 16 March 2015)

Recent experimental explorations of silicon nanomeshes have shown that the unique metastructures exhibit reduced thermal conductivity while preserving bulk electrical conductivity via feature sizes between relevant phonon and electron mean free paths, aiding in the continued promise that nanometer-scale engineering may further enhance thermoelectric behavior. Here, we introduce a strategy for tuning thermoelectric transport phenomena in semiconductor nanomeshes via heterogeneous elastic strain engineering, using silicon as a model material for demonstration of the concept. By combining analytical models for electron mobility in uniformly stressed silicon with finite element analysis of strained silicon nanomeshes in a lumped physical model, we show that the nonuniform and multiaxial strain fields defined by the nanomesh geometry give rise to spatially varying band shifts and warping, which in aggregate accelerate electron transport along directions of applied stress. This allows for global electrical conductivity and Seebeck enhancements beyond those of homogenous samples under equivalent far-field stresses, ultimately increasing thermoelectric power factor nearly 50% over unstrained samples. The proposed concept and structures—generic to a wide class of materials with large dynamic ranges of elastic strain in nanoscale volumes—may enable a new pathway for active and tunable control of transport properties relevant to waste heat scavenging and thermal management. © *2015 AIP Publishing LLC*. [http://dx.doi.org/10.1063/1.4915270]

Ever-increasing energy demands underscore the need for efficient waste heat recovery, and nanostructured thermoelectric materials are an increasingly attractive means to this end. Recent advances have shown enhanced thermoelectric figures-of-merit[1–3] (zT) in materials previously known for their bulk performance; however, these materials are commonly compound semiconductors incorporating rare or toxic elements, limiting their potential and adoption rates. Nanopatterned semiconductors and silicon, in particular, are recent recipients of increased attention[4–6] for their potential in frustrating phonon propagation and reducing thermal conductivity without adversely affecting electrical conductivity,[4] but conflicting studies promoting both phononic crystal effects[5] and diffuse scattering mechanisms[7] as the root causes of thermal conductivity reduction have hampered ultimate optimization of pattern size, shape, and spacing. Furthermore, the product of electrical conductivity and Seebeck coefficient squared ($\rho^{-1}S^2$, known as the thermoelectric power factor) remains unoptimized, hindering the potential of nanomeshes as a viable morphology for thermoelectric devices. Here, we introduce the concept of tunable *metadefect structures* by considering the effects of engineered elastic strain gradients around ordered features, patterned with length scales larger than the underlying atomic structure, on global electronic transport phenomena. In analogy to atomic-level defects in crystalline materials that introduce heterogeneous and long-range elastic strain fields owing to perturbations of the otherwise perfect crystalline lattice, we exploit strain amplification around patterned metadefects that give rise to changes in the electronic band structure to enhance transport. We focus our study on silicon, the most well understood semiconductor, to illustrate the metadefect concept and its potential for improving material performance through careful engineering of metastructure and resulting strain state.

Uniform elastic strain in bulk silicon has long been known to alter electron effective mass, mobility, and thus conductivity[8–12] leading to applications in high frequency field effect transistors. However, the role of intentionally introduced strain gradients and heterogeneity has received less attention. We propose the juxtaposition of elastic strain and rational spatial patterning of strain gradients via nanomesh geometries as a means of exploiting heterogeneity and control of the strain state. We extend these concepts beyond charge carrier mobility and, in the context of thermoelectric properties, consider the influence of spatial strain state heterogeneity on ρ^{-1}, S, and ultimately zT, given by

$$zT = \frac{\rho^{-1}S^2}{\kappa_e + \kappa_l}T, \tag{1}$$

where κ_e is the electronic contribution to thermal conductivity, κ_l is the phonon contribution to thermal conductivity, and T is temperature. To develop a quantitative description of the transport behavior via metadefects, a flexible geometric model incorporating the strain dependence of electronic band structure is required.

Here, we present a numerical method for calculating the thermoelectric-figure-of-merit in strained silicon nanomeshes. Beginning with an analytical model for electron mobility in arbitrarily strained n-type silicon, we utilize strain states obtained via finite element methods to compute electron

a)Author to whom correspondence should be addressed. Electronic mail: gianola@seas.upenn.edu

conductivity alongside Seebeck coefficients on an elemental level before determining global transport behavior. Through a systematic exploration of strain state, pattern, and hole geometry, we find optimized thermoelectric power factors for mesh porosities greater than 15%, as well as compute the dependence of optimal power factor on both applied stress magnitude and free electron concentration. These results bolster elastic strain engineering of semiconductor nanomeshes as a methodology for achieving tunable response, and serve to further highlight the importance of nanostructuring to the future of thermoelectric materials development.

We begin by treating the effect of strain state on electron mobility μ_e informed by the effective mass tensor, upon which the components of zT depend. In an n-type semiconductor, $\rho^{-1} = en\mu_e$, and the Wiedemann-Franz law[13] yields κ_e from ρ^{-1}, illustrating the increasing contribution of κ_e to total thermal conductivity with increasing carrier contribution. We also treat changes to S under the influence of elastic strain, which in the energy-independent scattering approximation, assuming parabolic band structure,[14] is given by[15]

$$S = \frac{8\pi^2 k_B^2}{3eh^2} m^*_{dos} T \left(\frac{\pi}{3n}\right)^{2/3}, \tag{2}$$

where n is carrier concentration and $m^*_{dos} = M_c^{2/3}(m_l m_t m_t)^{1/3}$ is the density-of-states effective mass, where M_c is the number of equivalent band minima, m_l is longitudinal effective mass, and m_t is transverse effective mass. Considering the fundamental dependence of both S and μ_e on effective mass, it is prudent to utilize explicit, tensorial models for this quantity as a function of strain.

To this end, we utilize a series of three recent analytical studies[16–18] predicated on treating electron mobility as a product of scalar scattering and tensorial effective mass components as the foundation for our modeling of transport in nanomeshes. The coalesced mobility model (our own implementation made explicit in the supplementary material[35]) is analytical and fully tensorial, taking into account strain-dependent changes to intervalley, intravalley, and impurity scattering rates,[16] changes to absolute bandgap width via deformation potential theory and band splitting,[17,18] as well as changes to electron effective mass due to band warping parameterized using the empirical pseudopotential method.[18] After modeling the effects of strain on these physical phenomena and calculating three Δ conduction-valley-pair-specific mobility tensors, the three tensors are weighted by the electron population of each valley pair to produce a final material mobility tensor for the input strain state. Through numerical implementation of the model we have independently verified the previous authors' results as largely self-consistent. We focus our attention here to global transport along $\langle 110 \rangle$ in Si, which has been shown to be the optimal transport direction when coincident with uniaxial stress.[19]

Fig. 1(a) illustrates the implementation of the aforementioned mobility model to a uniformly strained bulk silicon sample of carrier concentration $10^{19}\,\mathrm{cm}^{-3}$ at room temperature, showing enhancement of ρ^{-1} along [110] with respect to unstrained silicon for a varying in-plane uniaxial stress applied along the indicated crystallographic directions. In calculating S, we account for the breaking of silicon's sixfold degeneracy owing to strain and again weight the band-specific results by electron population in analogy with the coalesced mobility model.[20] For the case of plane tensile stress in (001), twofold degenerate Δ_2 valleys are brought closer in energy; whereas fourfold degenerate Δ_4 valleys are spread further apart. This results in the net reduction in S shown in Fig. 1(b), showing symmetry about [010] due its dependence on m^*_{dos} in contrast to the full effective mass tensor dependence held by ρ^{-1}. Results coincide with the near-universal reduction in S under tensile strain reported elsewhere,[21] again illustrating that net increases in m_l and m_t are insufficient to counter the effects of broken degeneracy. Fig. 1(c) shows the result of combining these factors to examine the thermoelectric power factor $\rho^{-1}S^2$. Our results show that elastic strain can enhance and maximize power factor along $\langle 110 \rangle$ by ensuring applied stress is largely coincident. Taken as a whole, the gains in electron mobility in uniaxially strained silicon counter the degeneracy, leading to a maximum of ~50% enhancement under optimized conditions near $\sigma_\infty = 1.5\,\mathrm{GPa}$.

To extend this fully analytical analysis to transport evaluation of two-dimensional strained metadefect structures, we employ the volume filament lumped model approach,[22,23] whereby continuum systems subjected to electrical fields are treated as systems of discrete elements divided such that equal current flows through each filament. To begin this treatment, we first apply a remote stress along Si [110] to a periodic nanomesh structure via finite element methods, converting a remote uniaxial strain state to one with combined shear and normal components and spatially altering the electronic band structure via unit cell volume changes, distortions, and symmetry breaking. We extract the full strain tensor at every node in the simulation, and this strain tensor is then used to calculate the electrical conductivity tensor ρ_{ij}^{-1} and S at each node using the model previously described, providing spatial maps of varying local electronic properties in each array geometry. To calculate charge transport through the nanomeshes and determine appropriate boundaries in volume filament division, a potential difference is also applied along [110], and isocurrent lines with inter-line spacing inversely proportional to the electron population are used to provide electron pathways of equal

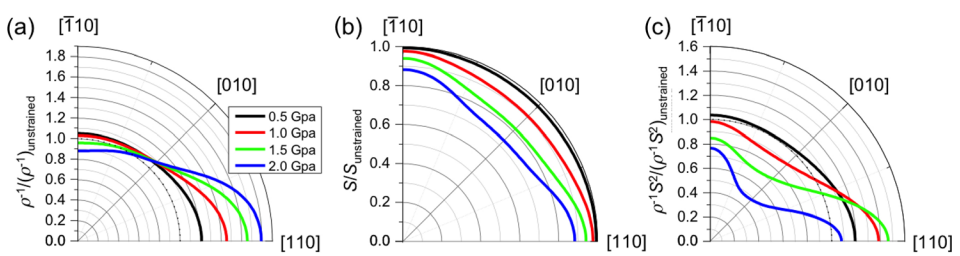

FIG. 1. Transport enhancement in fully dense silicon with respect to room temperature, unstrained silicon of carrier concentration $10^{19}\,\mathrm{cm}^{-3}$, of electrical conductivity (a), Seebeck coefficient (b), and thermoelectric power factor (c) as measured along [110] as a function of both magnitude and direction of applied uniaxial tensile stress.

current in the strained structures. This results in a continuous volume filament path along which ρ^{-1} can now be evaluated through equivalent circuit analysis (supplementary Fig. S1 (Ref. 35)), assuming nanomesh features are significantly larger than the electron mean free path[24] and total current is roughly equal to a similarly strained fully dense structure.[4] With spatial maps of ρ_{ij}^{-1} and electrical current pathways, then, we have all the information needed for discretizing the metadefect structure and integrating aggregate electron transport properties across the spatial domain.

Fig. 2 presents the results of our model for (001) *n*-silicon nanomeshes with an electron concentration of $10^{19}\,\mathrm{cm}^{-3}$, shown for both square (Fig. 2(a)) and diamond (Fig. 2(b)) arrays of cylindrical holes of equal porosity (lattice parameter 400 nm, porosity of 22%) under a remotely applied uniaxial stress of $\sigma_\infty = 1$ GPa. In these figures, individual colored lines are isocurrent density lines, where color represents the local electrical conductivity tensor at each node evaluated along the direction of electrical current transport. The equivalent electrical conductivity for each volume filament line is presented to the bottom of each figure, represented using the same color scale as the two unit cell images. Both geometries result in clear conductivity enhancements owing to elastic deformation, particularly in regions surrounding large tensile stresses. Interestingly, they differ in producing notably different spatial conductivity maps, with sharper spatial gradients apparent in the square unit cell. The deformed diamond array leads to larger values of shear strain between holes (supplementary Fig. S2 (Ref. 35)), giving rise to stronger band warping in these regions. Remarkably, global effective conductivities for the square and diamond nanomesh structures are 283 S/cm (56% enhancement relative to the unstrained material) and 272 S/cm (50% enhancement), respectively. Provided thermal conductivities that are roughly equivalent (as assumed from equal porosities and features well above thermal phonon mean free paths),[7] the fact that one structure produces greater local conductivity enhancements, while the other global, provides added flexibility in choosing the best geometry for a given application.

In utilizing this model for global electrical conductivity in conjunction with global Seebeck coefficients (obtained by averaging local Seebeck coefficients along isocurrent paths[25]), we are now equipped to make a semi-quantitative comparison between the two nanomesh structures as functions of remote stress and carrier concentration to guide experimental implementation. As seen in Figs. 3(a) and 3(b), $\rho^{-1}S^2$ enhancement relative to unstrained silicon for both sample geometries at 22% porosity is shown, using the Goldsmid expression for Seebeck coefficient[26] with constant scattering parameter $r = -1/2$ allowing comparison across a wide range of dopant concentrations. Immediately apparent is that $\rho^{-1}S^2$ is enhanced substantially over unstrained material and the concentration at which $\rho^{-1}S^2$ is maximized decreases with increasing stress for both geometries, starting at 6.5×10^{18} cm^{-3} for unstrained silicon and dropping as low as 2.7×10^{18} cm^{-3} for $\sigma_\infty = 2$ GPa, due to Δ_4 depopulation at higher stresses causing a gradual reduction in S at lower n. Also of note is the near-identical behavior predicted for both geometries at applied stresses up to $\sigma_\infty = 0.5$ GPa, and the fact that the stress at which $\rho^{-1}S^2$ is maximized ($\sim$1 GPa) is substantially reduced in comparison with unpatterned material ($\sim$1.5 GPa). This points toward the geometries remaining functionally identical at more easily achieved applied stresses, meaning experimental realization of an optimized strained nanomesh should be possible. In particular, we note the clear advantage of using nanoscale geometries beyond the effects of phonon scattering leading to beneficial reductions of thermal conductivity for thermoelectric applications. Namely, the use of small volumes leads to tremendous gains in strength and thus elastic range prior to plastic deformation or fracture,[27] ensuring fully reversible and tunable behavior over a large number of cycles. The diamond lattice structure may ultimately be at a practical disadvantage due to $\sim$40% higher peak strains at hole edges from smaller radii of curvature compared to a square lattice of equal porosity, rendering the structures more susceptible to failure at the same level of thermoelectric performance. Nevertheless, if care is taken to not exceed the elastic limit of nanostructured Si, then the phenomena elucidated here are entirely reversible and thus tunable for a given application or temperature.

With maximized carrier concentration and remote stresses determined, further optimization can be found by varying the porosity for each geometry and computing global

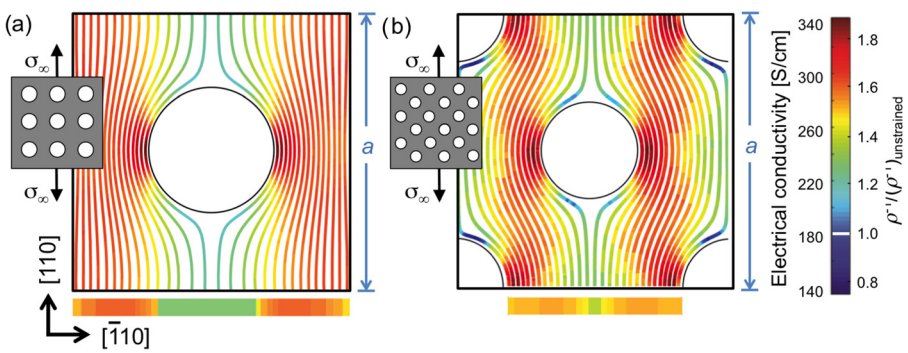

FIG. 2. Simulation results for strained silicon nanomeshes indicating instantaneous electrical conductivity evaluated along lines of constant current in square (a) and diamond (b) 400 nm lattice parameter a unit cells under $\sigma_\infty = 1$ GPa remote uniaxial stress along [110], as calculated from the full electron mobility tensor at each point, at room temperature. Color bars below (a) and (b) indicate the effective electrical conductivity for each line, and the global effective conductivities for the two 22% porosity structures are 282.5 S/cm (55.6% enhancement) and 271.8 S/cm (49.9% enhancement), respectively. Effective conductivities are calculated via lumped modeling by applying equivalent circuit analysis across nodes, summing elements in series horizontally and in parallel vertically. Reported percent enhancement is with respect to unstrained, bulk silicon with a carrier concentration of $10^{19}\,\mathrm{cm}^{-3}$.

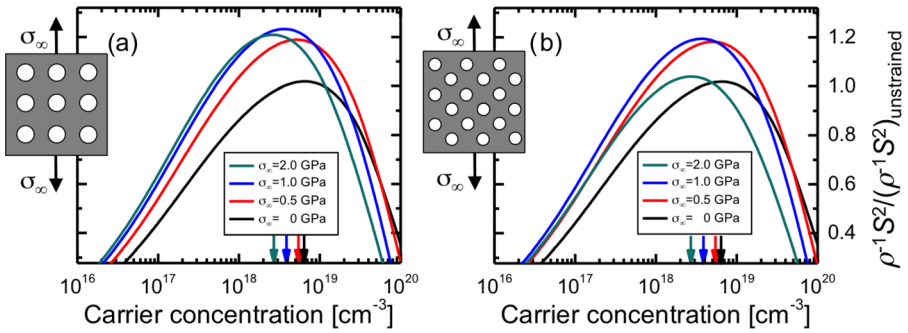

FIG. 3. Power factor ($\rho^{-1}S$) as a function of carrier concentration and applied uniaxial stress along [110] for square (a) and diamond lattice (b) silicon nanomeshes, as evaluated at room temperature. All curves are normalized to the maximum power factor of the unstrained silicon nanomesh. The carrier concentrations for which $\rho^{-1}S$ is maximized for each condition are indicated with colored arrows. For the purpose of comparison across a wide range of carrier concentrations, this figure relies on the Seebeck formula laid out by Goldsmid[26] using constant scattering parameter $r = -1/2$.

quantities at the optimized conditions $\sigma_\infty = 1$ GPa and $n = 3.8 \times 10^{18}$ cm^{-3}. As shown in Fig. 4(a), smaller porosity values ($0.15 < \phi < 0.25$, keeping porosity constant and varying pattern lattice parameter) result in roughly equivalent ρ^{-1} enhancements, but the two structures surprisingly trend in opposite directions as porosity is increased beyond $\phi > 0.25$. Global effective S values (Fig. 4(b)) follow the reverse trends. With these results combined (Fig. 4(c)), $\rho^{-1}S^2$ of the square lattice increases monotonically with increasing ϕ over the range simulated, showing enhancements near 50% over unstrained silicon, giving 5.75 W m^{-1} K^{-2} for the modest applied stress $\sigma_\infty = 1$ GPa, while the diamond lattice exhibits a reduction in $\rho^{-1}S^2$ corresponding directly with the reduced ρ^{-1} shown in Fig. 4(a). Further increases in porosity beyond those reported in Fig. 4 would lead to ligament widths that are <50 nm and begin to approach the regime where surface scattering of electrons would also reduce $\rho^{-1}S^2$ of the unstrained nanomesh. Thus, the focus of this study is on the tunable parameter of strain.

These results indicate that the square nanomesh array not only provides larger global transport enhancements for the same applied remote stress but also robust behavior over a wide range of porosities. The drastic reduction in both S and ρ^{-1} visible at higher porosities in the diamond lattice structure may be explained by the more tortuous paths and distinct cumulative strain states experienced by electrons travelling through the structure. Higher average transport path curvature results in electrons travelling nearly constantly at an angle 45° to the direction of applied stress in the proximity of the pores, where as shown in Fig. 1(a), all factors are enhanced the least with respect to unstrained silicon. Likewise, S values in Fig. 1(b) cross from a minimum when the direction of measured transport is 45° to the direction of applied stress back towards a local maximum when stress and transport are perpendicular. As shown in supplementary Fig. S3,[35] both maximum local strain magnitudes and the proportion of current forced through the regions of high tensile strain increase as a function of porosity. Assuming total current remains constant, these results show that strain amplification and heterogeneity have a net positive effect on $\rho^{-1}S^2$.

Taken as a whole, the strain amplification and spatial heterogeneity in Si nanomeshes can yield improved power factors, yet these geometries should also affect thermal conductivity. Using our quantitative descriptions of electron transport in strained silicon nanomeshes, we now make a number of reasonable assumptions regarding thermal transport to estimate zT in such metadefect structures. To start, we conservatively assume strain-invariant κ_l over the elastic range studied,[28,29] negligible κ_e, and neglect changes to array lattice parameter as a result of elastic strain (which would be smaller than 0.59% for 1 GPa applied stress). With regards to

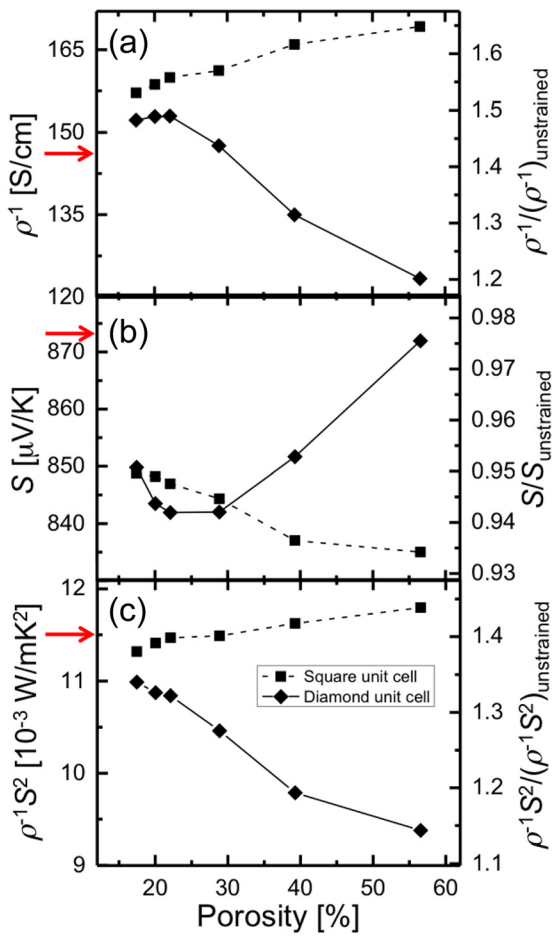

FIG. 4. Room temperature electrical conductivity (a), Seebeck coefficient (b), and effective power factor (c) of square and diamond lattice silicon nanomeshes as functions of mesh porosity for $\sigma_\infty = 1$ GPa applied uniaxial stress along [110] and $n = 3.8 \times 10^{18}$ cm^{-3}. Reported percent enhancement is with respect to unstrained, bulk silicon with a carrier concentration of $n = 3.8 \times 10^{18}$cm^{-3}, also at room temperature, and red arrows at left indicate values for bulk strained silicon with a carrier concentration of $n = 3.8 \times 10^{18}$cm^{-3} at room temperature.

κ_l, we recognize that exact mechanisms behind the reported reductions in nanomeshes are still under debate. In addition, the critical dimensions that govern transport are still not clear, with researchers promoting either minimum neck width[24,30] or feature spacing and periodicity.[4,5] We conservatively consider only nanomeshes with feature sizes above the electron mean free path in highly doped silicon (1–10 nm) where there should be no significant reduction in device conductivity or sharpening of density of states.[24] Thus, for the porosity ranges studied here, we expect the unstrained nanomeshes to exhibit bulk-like electrical conductivity, consistent with experimental measurements on Si nanomeshes.[4] Applying $\sigma_\infty = 1$ GPa to the structures fabricated by Tang *et al.*[24] (diamond lattice, lattice constant $a = 55$ nm, $\phi = 0.35$, $n = 5 \times 10^{19}$ cm^{-3}, $\kappa_l = 1.73$ W m^{-1} K^{-1}), we estimate a power factor of 0.536 m K W^{-1} and zT of 0.31 at room temperature. We note that even this enhancement is modest, as the experimental conditions do not coincide with our calculated optimal lattice type, porosity, or carrier concentration. Employing the phonon mean free path-centric approach advanced by Jain *et al.*[7] allows a rough zT comparison between the square and diamond unit cell geometries by assuming that κ_l for both should be comparable for a given porosity. The same set of parameters instead applied to a square lattice with $n = 3.8 \times 10^{18}$ cm^{-3} yields a power factor of 2.68 m K W^{-1} and zT of 1.55 at room temperature assuming the near-amorphous-limit reported κ_l holds valid, producing an enhancement over two orders of magnitude with respect to bulk, unstrained silicon ($zT = 0.01$).[31]

We note that our results suggest optimized metadefect structures with pore sizes, carrier concentrations, and remote strains that are experimentally within reach for both free-standing[32] and bound top-down[33] silicon structures. It is also important to reiterate that strained silicon has been discussed here as a model system; the principles introduced here could be easily extended to other material systems. Details of electron and phonon band structures are of course material-dependent, but the simultaneous frustration of phonon propagation and enhancement of electron transport discussed here should be possible wherever metadefect structures are employed at length scales larger than electron mean free paths. We predict that materials showing large band shifts and warping, in addition to strain-mediated degeneracy[34] would be promising avenues to pursue. Thermoelectric power factor is universally reduced at higher stresses, suggesting that any approach towards tuning $\rho^{-1}S^2$ in heterostructures may benefit most from an optimization of σ_∞ that would likely differ from the uniaxial scenario, where stress amplification from metadefects could cause local reductions in $\rho^{-1}S^2$ and ultimately reduce global values. We also note that optimizing the pore geometry (e.g., ellipticity) in addition to that of the pore array would provide an additional degree of freedom for transport enhancement.

In summary, we find that elastic strain gradients in strained Si nanomeshes enable highly tunable thermoelectric power factors and potential zT enhancements two orders of magnitude greater than that of unstrained, bulk material. We expect this avenue to be particularly promising in nanostructures, which often provide unprecedented material strengths near the theoretical upper limit and thus a large range of dynamic range of elastic strain over which to control transport phenomena.

This research was supported by the U.S. Department of Energy, Office of Basic Energy Sciences, Division of Materials Science and Engineering under Award #DE-SC0008135. The authors would like to thank Yaohua Tan for discussions of his contribution to the electron mobility model, and Kathryn F. Murphy for her aid in figure production and critical reading of the manuscript.

[1]B. Poudel, Q. Hao, Y. Ma, Y. Lan, A. Minnich, B. Yu, X. Yan, D. Wang, A. Muto, D. Vashaee, X. Chen, J. Liu, M. S. Dresselhaus, G. Chen, and Z. Ren, Science **320**, 634–638 (2008).
[2]C.-L. Chen, Y.-Y. Chen, S.-J. Lin, J. C. Ho, P.-C. Lee, C.-D. Chen, and S. R. Harutyunyan, J. Phys. Chem. C **114**, 3385–3389 (2010).
[3]Y. Ma, Q. Hao, B. Poudel, Y. Lan, B. Yu, D. Wang, G. Chen, and Z. Ren, Nano Lett. **8**, 2580–2584 (2008).
[4]J.-K. Yu, S. Mitrovic, D. Tham, J. Varghese, and J. R. Heath, Nat. Nanotechnol. **5**, 718–721 (2010).
[5]P. E. Hopkins, C. M. Reinke, M. F. Su, R. H. Olsson, E. A. Shaner, Z. C. Leseman, J. R. Serrano, L. M. Phinney, and I. El-Kady, Nano Lett. **11**, 107–112 (2010).
[6]J.-H. Lee, G. A. Galli, and J. C. Grossman, Nano Lett. **8**, 3750–3754 (2008).
[7]A. Jain, Y.-J. Yu, and A. J. H. McGaughey, Phys. Rev. B **87**, 195301 (2013).
[8]M. Fischetti, F. Gamiz, and W. Hansch, J. Appl. Phys. **92**, 7320–7324 (2002).
[9]S. E. Thompson, M. Armstrong, C. Auth, M. Alavi, M. Buehler, R. Chau, S. Cea, T. Ghani, G. Glass, and T. Hoffman, IEEE Trans. Electron Devices **51**, 1790–1797 (2004).
[10]M. L. Lee, E. A. Fitzgerald, M. T. Bulsara, M. T. Currie, and A. Lochtefeld, J. Appl. Phys. **97**, 011101 (2005).
[11]B. Y. Tsaur, J. C. Fan, and M. Geis, Appl. Phys. Lett. **40**, 322–324 (1982).
[12]G. Abstreiter, H. Brugger, T. Wolf, H. Jorke, and H. Herzog, Phys. Rev. Lett. **54**, 2441 (1985).
[13]R. Franz and G. Wiedemann, Ann. Phys. **165**, 497–531 (1853).
[14]M. Cutler, J. F. Leavy, and R. L. Fitzpatrick, Phys. Rev. **133**, A1143–A1152 (1964).
[15]G. J. Snyder and E. S. Toberer, Nat. Mater. **7**, 105–114 (2008).
[16]S. Dhar, H. Kosina, V. Palankovski, S. E. Ungersboeck, and S. Selberherr, IEEE Trans. Electron Devices **52**, 527–533 (2005).
[17]S. Dhar, E. Ungersbock, H. Kosina, T. Grasser, and S. Selberherr, IEEE Trans. Nanotechnol. **6**, 97–100 (2007).
[18]Y. Tan, X. Li, L. Tian, and Z. Yu, IEEE Trans. Electron Devices **55**, 1386–1390 (2008).
[19]H. Irie, K. Kita, K. Kyuno, and A. Toriumi, IEDM Tech. Dig. **2004**, 225–228.
[20]T. Manku and A. Nathan, IEEE Trans. Electron Devices **39**, 2082–2089 (1992).
[21]N. F. Hinsche, I. Mertig, and P. Zahn, J. Phys.: Condens. Matter **23**, 295502 (2011).
[22]S. Mei and Y. I. Ismail, IEEE Trans. VLSI **12**, 437–447 (2004).
[23]S. Kim and D. P. Neikirk, IEEE MTT-S **3**, 1815–1818 (1996).
[24]J. Tang, H.-T. Wang, D. H. Lee, M. Fardy, Z. Huo, T. P. Russell, and P. Yang, Nano Lett. **10**, 4279–4283 (2010).
[25]R. Kim and M. S. Lundstrom, J. Appl. Phys. **110**, 034511 (2011).
[26]H. J. Goldsmid, *Electronic Refrigeration* (Pion, 1986).
[27]Y. Zhu, F. Xu, Q. Qin, W. Y. Fung, and W. Lu, Nano Lett. **9**, 3934–3939 (2009).
[28]K. F. Murphy, B. Piccione, M. B. Zanjani, J. R. Lukes, and D. S. Gianola, Nano Lett. **14**, 3785–3792 (2014).
[29]X. Li, K. Maute, M. L. Dunn, and R. Yang, Phys. Rev. B **81**, 245318 (2010).
[30]Q. Hao, G. Chen, and M.-S. Jeng, J. Appl. Phys. **106**, 114321 (2009).
[31]L. Weber and E. Gmelin, Appl. Phys. A **53**, 136–140 (1991).
[32]M. M. Roberts, L. J. Klein, D. E. Savage, K. A. Slinker, M. Friesen, G. Celler, M. A. Eriksson, and M. G. Lagally, Nat. Mater. **5**, 388–393 (2006).
[33]R. A. Minamisawa, M. J. Süess, R. Spolenak, J. Faist, C. David, J. Gobrecht, K. K. Bourdelle, and H. Sigg, Nat. Commun. **3**, 1096 (2012).
[34]Y. Pei, X. Shi, A. LaLonde, H. Wang, L. Chen, and G. J. Snyder, Nature **473**, 66–69 (2011).
[35]See supplementary material at http://dx.doi.org/10.1063/1.4915270 for a detailed description of the electron mobility and equivalent circuit models.